The effect of spherical additives on a liquid crystal colloid

2004 J. Phys.: Condens. Matter 16 S1887

(http://iopscience.iop.org/0953-8984/16/19/002)

INSTITUTE OF PHYSICS PUBLISHING JOURNAL OF PHYSICS: CONDENSED MATTER

J. Phys.: Condens. Matter **16** (2004) S1887–S1900 PII: S0953-8984(04)75611-8

The effect of spherical additives on a liquid crystal colloid

Dmytro Antypov[1] **and Douglas J Cleaver**[2]

[1] Max Planck Institute for Polymer Research, D-55021, Mainz, Postfach 3148, Germany
[2] Materials Research Institute, Sheffield Hallam University, Pond Street, Sheffield S1 1WB, UK

Received 29 January 2004
Published 30 April 2004
Online at stacks.iop.org/JPhysCM/16/S1887
DOI: 10.1088/0953-8984/16/19/002

Abstract

We present a computer simulation study of a colloidal particle immersed in a solvent comprising liquid crystalline rod-shaped particles and a 10% number concentration of small spherical additives. The presence of the colloidal particle (and its periodic images) is found to induce qualitative changes in the phase behaviour of the rod–sphere mixture. When the colloidal particle favours radial anchoring, it is found that the small spheres spontaneously aggregate to form a droplet which resides in the equatorial plane of the colloidal particle. When the colloidal particle favours tangential anchoring, however, the small spheres aggregate to form droplets at each of the boojums seen experimentally. These findings confirm expectations that small additives to liquid crystalline systems should preferentially reside in disordered regions, whilst also reflecting the competing influence of surface tension effects.

(Some figures in this article are in colour only in the electronic version)

1. Introduction

Since the pioneering work of Asakura and Oosawa [1], much effort has gone into understanding the interactions governing the behaviour of complex colloidal systems. For example, it is known that spherical colloidal particles in a suspension containing low concentrations of rod-like colloids experience an enhanced depletion-induced effective attraction [2]. If the radius of the colloid is R and the length of the rod is l, there is a depletion zone of thickness $l/2$ around the colloid in which the allowed rod orientations are restricted. When two colloids approach each other, their depletion zones overlap further, and the resultant increase in the rods' entropy leads to an effective attractive force between the colloids [3].

In contrast, for systems in which the rods are much smaller than the spheres, such as liquid crystal (LC) colloids, most models neglect the microscopic details of the LC, representing it instead with a continuum property such as the director field $\hat{\mathbf{n}}(\mathbf{r})$. Provided that changes in $\hat{\mathbf{n}}(\mathbf{r})$ occur on length scales larger than the molecular size, the free energy cost associated with such deformations can be characterized (in the one-constant approximation) by an averaged

Frank constant K. For a spherical colloid with radial boundary conditions, a topological mismatch is created between the director fields near to and far from the colloid. The resultant deviations from a uniform director field are balanced by surface energy terms characterized by the anchoring energy W [4]. If $WR/K \ll 1$ the anchoring is weak and the bulk elasticity prevails over the surface energy. The director field in this case is only slightly distorted. If $WR/K \gg 1$, however, the anchoring is strong and a number of director arrangements are possible including a quadrupolar Saturn ring structure and a dipolar structure with a satellite defect [5]. The relative stabilities of these structures depend critically on the core energies of any disclination ring and/or point defects present, however, an issue that is difficult to resolve at a continuum level.

A range of computer simulation methods have been employed to assess the director field distortions near a colloidal particle. Mesoscopic models have been used to determine, in three dimensions, the director field around a single colloid [6] and to simulate, in two dimensions, the aggregation of several colloids due to director-field mediated interactions [7, 8]: these models are only able to represent the defects at a coarse-grained level, however. Microscopic results have also been obtained for relatively small three-dimensional systems with a single colloidal particle. For example, a Saturn ring defect was observed by Billeter and Pelcovits [9] in a system of 2048 Gay–Berne particles of dimension $1\sigma_0$ by $3\sigma_0$ and a spherical colloid of diameter $3\sigma_0$. A similar system was studied by Andrienko and Allen [10] using up to a million soft Gaussian overlap particles and a single colloid up to $30\sigma_0$ in diameter. Here it was found that, for radial anchoring, only the Saturn ring defect remained stable at small colloid sizes. The satellite defect proved unstable over simulation timescales unless the colloid diameter was increased to $30\sigma_0$. From density and order parameter maps measured in this study, the position of the core region of the ring defect in these simulations was found to be a linear function of the colloid radius R. For relatively small colloids, the defect was located very close to the colloid surface: for $R = 3.0\sigma_0$, for example, the estimated radius of the defect was $R_d = 3.162\sigma_0$. The order parameter profiles from [10] also indicated no irregularities at distances larger than $4\sigma_0$ from the colloid surface. This implies that large simulation box sizes are not needed when simulating LC colloid systems with Saturn ring defects.

In this paper, we use molecular dynamics (MD) simulations performed in the constant NVT ensemble to investigate the effect of small spherical additives on the director structures adopted in the vicinity of a LC colloid. Here, the microscopic details of the LC molecules are paramount in determining the behaviour of the small spheres, whereas the director field perspective offers the clearest description of the resultant effect on colloid–colloid interactions. It has been argued [11] and, more recently, observed [12] that isotropic particles in a LC preferentially reside in regions of director distortion (such as defects) so as to relieve the high elastic energy densities found therein. There is interest, therefore, in employing appropriately tuned additives to control the defects that underpin, for example, the string-of-pearls LC colloid structure. By the same token, it is possible that in any practical applications of LC colloids, system degradation might lead to a gradual build-up of small unwanted molecular fragments. It is, therefore, relevant to assess the possible effects of such fragments on model LC colloid systems. The remainder of this paper is organized as follows. In section 2 we describe the interaction potentials used in the simulations, paying particular attention to those involving the colloidal particle. Simulation results for both radially anchored and tangentially anchored LC colloids are then presented and discussed in section 3 before conclusions are drawn in section 4.

2. Model systems

In this study, we assess the effect of small spherical additives on the director field around a LC colloid. To do this, we employ molecular models which are well characterized in the single

component limit: for the sphere–sphere and rod–rod interactions, we use the Lennard-Jones and Gay–Berne potentials, respectively. The former is given by

$$U^{\mathrm{LJ}}(r_{ij}) = 4\epsilon_0 \left(\left(\frac{\sigma_0}{r_{ij}} \right)^{12} - \left(\frac{\sigma_0}{r_{ij}} \right)^{6} \right), \tag{1}$$

where σ_0 and ϵ_0 are constants that set the length and energy scales and r_{ij} is the separation of particles i and j. The Gay–Berne interaction between a pair of rod-like molecules is given by

$$U^{\mathrm{GB}}(\mathbf{r}_{ij}, \hat{\mathbf{u}}_i, \hat{\mathbf{u}}_j) = 4\epsilon(\hat{\mathbf{r}}_{ij}, \hat{\mathbf{u}}_i, \hat{\mathbf{u}}_j) \left[\left(\frac{\sigma_0}{r_{ij} - \sigma(\hat{\mathbf{r}}_{ij}, \hat{\mathbf{u}}_i, \hat{\mathbf{u}}_j) + \sigma_0} \right)^{12} - \left(\frac{\sigma_0}{r_{ij} - \sigma(\hat{\mathbf{r}}_{ij}, \hat{\mathbf{u}}_i, \hat{\mathbf{u}}_j) + \sigma_0} \right)^{6} \right], \tag{2}$$

where $\hat{\mathbf{r}}_{ij} = \mathbf{r}_{ij}/r_{ij}$ is a unit vector along the intermolecular vector $\mathbf{r}_{ij} = \mathbf{r}_i - \mathbf{r}_j$ and the unit vectors $\hat{\mathbf{u}}_i$ and $\hat{\mathbf{u}}_j$ denote the rod orientations. Full expressions for the shape anisotropy parameter, $\sigma(\hat{\mathbf{r}}_{ij}, \hat{\mathbf{u}}_i, \hat{\mathbf{u}}_j)$, and the well-depth anisotropy function, $\epsilon(\hat{\mathbf{r}}_{ij}, \hat{\mathbf{u}}_i, \hat{\mathbf{u}}_j)$, are given in the standard references [13, 14].

Here, we set the diameters of the small spheres and the breadths of the rods equal to the same constant σ_0. Similarly, we equate the well depths of the rod–rod cross arrangement and sphere–sphere interactions at ϵ_0. Finally, the Gay–Berne model contains four adjustable parameters: the elongation l/σ_0, the energy anisotropy $\epsilon_{\mathrm{side-side}}/\epsilon_{\mathrm{end-end}}$ and the exponents μ and ν. Here, we adopt the frequently used parametrization $l/\sigma_0 = 3$, $\epsilon_{\mathrm{side-side}}/\epsilon_{\mathrm{end-end}} = 5$, $\mu = 2$ and $\nu = 1$ for which the bulk phase behaviour is well established [14].

For the rod–sphere potential, we employ equation (2), taking the appropriate limit of $\sigma(\hat{\mathbf{r}}_{ij}, \hat{\mathbf{u}}_i, \hat{\mathbf{u}}_j)$ originally noted by Berne and Pechukas [15]. Thus, for the case where particle j is a rod and particle i is a sphere with diameter equal to the rod's breadth, the shape parameter is expressed as

$$\sigma(\hat{\mathbf{r}}_{ij}, \hat{\mathbf{u}}_j) = \sigma_0[1 - \chi(\hat{\mathbf{r}}_{ij} \cdot \hat{\mathbf{u}}_j)^2]^{-1/2} \tag{3}$$

where

$$\chi = \frac{(l/\sigma_0)^2 - 1}{(l/\sigma_0)^2 + 1}. \tag{4}$$

The energy parameter we adopt for the rod–sphere interaction is

$$\epsilon(\hat{\mathbf{r}}_{ij}, \hat{\mathbf{u}}_j) = \epsilon_0[1 - \chi'(\hat{\mathbf{r}}_{ij} \cdot \hat{\mathbf{u}}_j)^2]^{\mu}, \tag{5}$$

where

$$\chi' = \left(1 - \left(\frac{\epsilon_{\mathrm{E}}}{\epsilon_{\mathrm{S}}} \right)^{1/\mu} \right) \tag{6}$$

and the ratio $\epsilon_{\mathrm{S}}/\epsilon_{\mathrm{E}}$ is the side-to-end well-depth anisotropy of the interaction. In this paper, set $\epsilon_{\mathrm{S}}/\epsilon_{\mathrm{E}} = \epsilon_{\mathrm{side-side}}/\epsilon_{\mathrm{end-end}} = 5$ such that the spheres favour the sides of the rods rather than the ends.

We now consider the colloid–rod and colloid–sphere interactions. The forms used to describe the colloid–rod potentials in [9] and [10] are both inadequate for our purposes here. The potential used in [10] takes a shifted Lennard-Jones form with no dependence on the rod's orientation. It, therefore, offers no scope for tuning of either the anchoring strength or the preferred anchoring direction. The potential used in [9] comprises two terms, one purely repulsive and the other controlling surface anchoring. Thus

$$U^{\mathrm{P}}(\mathbf{r}_{ij}, \hat{\mathbf{u}}_j) = 4\epsilon_{\mathrm{P}} \left(\frac{\sigma_0}{r_{ij} - \sigma(\hat{\mathbf{r}}_{ij}, \hat{\mathbf{u}}_j) + \sigma_0} \right)^{18} - W_{\mathrm{P}} \left(\frac{\hat{\mathbf{r}}_{ij} \cdot \hat{\mathbf{u}}_j}{r_{ij}} \right)^{6} \tag{7}$$

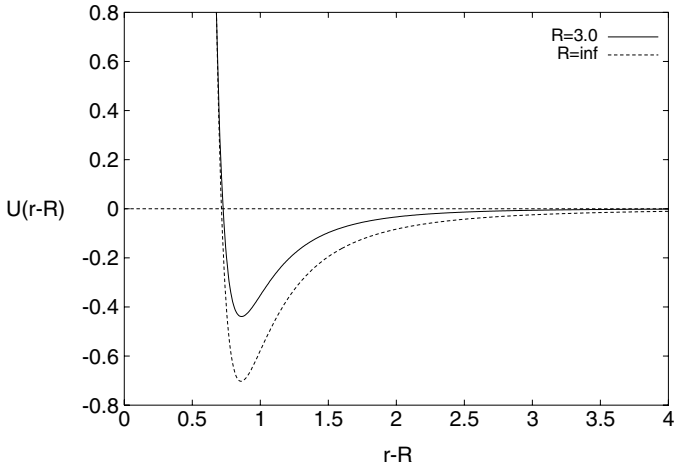

Figure 1. The colloid–sphere potential (equation (8)) for $R = 3\sigma_0$ and $R = \infty$ at $\epsilon_0^{\mathrm{CS}} = 4\epsilon_0$.

where the parameter W_{P} is a phenomenological anchoring coefficient. The exponent 18 instead of 12 was chosen here so as to reduce the active interaction region and make the repulsion 'harder'. However, equation (7) has no clear microscopic or intuitive basis for anchoring control.

We have, therefore, developed alternative potentials for the interactions between the small spherical and prolate particles and the large spherical colloid. For these, the large colloidal particle was considered as an assembly of smaller spherical particles taken to interact with a given external particle via a 6-12-power potential. Representing the colloid as an explicit multi-site object in a simulation would be an undesirable complication (and expense). Rather, we have developed pair-wise colloid–small-particle potentials by taking the colloid to be a continuum of Lennard-Jonesium and integrating over its volume. As shown in the appendix, for the colloid–sphere case, this leads to a potential of the form

$$U^{\mathrm{CS}}(r_{ij}) = \epsilon_0^{\mathrm{CS}}\left[\frac{{\sigma_0}^9}{45(r_{ij}-R)^9} - \frac{{\sigma_0}^3}{6(r_{ij}-R)^3} - \frac{{\sigma_0}^9}{40r_{ij}(r_{ij}-R)^8} + \frac{{\sigma_0}^9}{4r_{ij}(r_{ij}-R)^2}\right], \tag{8}$$

where ϵ_0^{CS} is a single adjustable parameter which can be taken to depend on the packing of the particles forming the colloid and on the strength of their interaction with an external particle. Figure 1 shows the colloid sphere potential for $R = 3\sigma_0$ and $\epsilon_0^{\mathrm{CS}} = 4\epsilon_0$ as an example. The dashed line in this figure corresponds to a 3–9 potential (commonly used to represent a semi-infinite planar substrate), which, we note, is the limit of expression (8) when $R = \infty$.

By employing Gay and Berne's [13] approach of supplementing the bracketed r_{ij} terms with a shifted orientation-dependent range parameter, the potential (8) can also be extended to give an interaction between the colloid and a non-spherical particle. This gives the following colloid–rod interaction:

$$\begin{aligned} U^{\mathrm{CR}}(\mathbf{r}_{ij},\hat{\mathbf{u}}_j) = \epsilon_{\mathrm{CR}}(\hat{\mathbf{r}}_{ij},\hat{\mathbf{u}}_j)\Bigg[&\frac{{\sigma_0}^9}{45(d_{ij}-\sigma_{\mathrm{CR}}(\hat{\mathbf{r}}_{ij},\hat{\mathbf{u}}_j)+\sigma_0)^9} - \frac{{\sigma_0}^3}{6(d_{ij}-\sigma_{\mathrm{CR}}(\hat{\mathbf{r}}_{ij},\hat{\mathbf{u}}_j)+\sigma_0)^3} \\ &- \frac{{\sigma_0}^9}{40r_{ij}(d_{ij}-\sigma_{\mathrm{CR}}(\hat{\mathbf{r}}_{ij},\hat{\mathbf{u}}_j)+\sigma_0)^8} + \frac{{\sigma_0}^3}{4r_{ij}(d_{ij}-\sigma_{\mathrm{CR}}(\hat{\mathbf{r}}_{ij},\hat{\mathbf{u}}_j)+\sigma_0)^2}\Bigg], \end{aligned} \tag{9}$$

where $d_{ij} = r_{ij} - R$,

$$\sigma_{\mathrm{CR}}(\hat{\mathbf{r}}_{ij}, \hat{\mathbf{u}}_j) = \sigma_0 \sqrt{\frac{1 - \chi \sin^2\theta}{1 - \chi}}, \tag{10}$$

and

$$\epsilon_{\mathrm{CR}}(\hat{\mathbf{r}}_{ij}, \hat{\mathbf{u}}_j) = \epsilon_0^{\mathrm{CR}} \left(\frac{1 - \chi'}{1 - \chi' \sin^2\theta} \right)^{\mu}. \tag{11}$$

Here, $\cos\theta = \hat{\mathbf{r}}_{ij} \cdot \hat{\mathbf{u}}_j$ and the parameters χ and χ' are the same as those defined for the rod–sphere interaction (equations (4) and (6), respectively). The expressions (10) and (11) were originally determined for a rod–plane system [16] but are adopted here on the basis that the colloid radius is sufficiently large for surface curvature effects on $\sigma_{\mathrm{CR}}(\hat{\mathbf{r}}_{ij}, \hat{\mathbf{u}}_j)$ and $\epsilon_{\mathrm{CR}}(\hat{\mathbf{r}}_{ij}, \hat{\mathbf{u}}_j)$ to be small.

3. Simulation results

All simulations presented here were performed using constant NVT MD on a 90/10 rod–sphere mixture containing 1844 Gay–Berne rods and 204 Lennard-Jones spheres (i.e. 2048 small particles in total). The MD code employed the velocity Verlet integrator [17] with a time step $\delta t = 0.0015\sqrt{m\sigma_0^2/\epsilon_0}$. At each state point, the system was equilibrated for at least 5×10^5 time steps followed by a production run of 2×10^5 time steps. Observables were calculated every 200 time steps and then averaged. Periodic boundary conditions, minimum image convention and Verlet neighbour lists were applied. All interaction potentials were truncated and shifted at a distance $r_c = 4\sigma_0$. The masses, m, of the rods and spheres were set to unity as were the moments of inertia about the short axes of the rods. The colloidal particle was treated as a static force field.

In the following, all quantities are expressed in reduced units. This means that distance is measured in units of σ_0, energy in units of ϵ_0 and temperature in units of $\epsilon_0/k_{\mathrm{B}}$, where k_{B} is Boltzmann's constant. As a consequence, $\sqrt{m\sigma_0^2/\epsilon_0}$ is the unit of time and the number density, ρ, is measured in units of σ_0^{-3}. The orientational order parameter, S, was monitored throughout the simulations, being calculated as the ensemble average of the largest eigenvalue of the Q tensor:

$$Q_{\alpha\beta} = \frac{1}{N_{\mathrm{rods}}} \sum_{i=1}^{N_{\mathrm{rods}}} \frac{1}{2}(3u_{i\alpha}u_{i\beta} - \delta_{\alpha\beta}), \tag{12}$$

where $u_{i\alpha}$ is the α component ($\alpha = x, y, z$) of $\hat{\mathbf{u}}_\mathbf{i}$ and $\delta_{\alpha\beta}$ is the Kronecker delta. Rod–rod, rod–sphere and sphere–sphere radial distribution functions were also calculated to assess any structural changes.

Before considering the behaviour of this 90/10 rod–sphere mixture in the presence of a colloidal particle, we first give a brief description of its phase behaviour in bulk. In a previous paper [18] it was shown that, in the hard-particle limit, this mixture simply undergoes a homogeneous nematic–isotropic transition at a slightly higher volume fraction than a pure 3:1 hard-Gaussian-overlap fluid. However, none of the lamellar and/or phase-separated behaviour found for more extreme rod anisotropies and higher sphere concentrations was exhibited by this system.

The bulk 90/10 rod–sphere system of Gay–Berne and Lennard-Jones particles was initially equilibrated for 7×10^5 times steps at the mixed, isotropic state point $T = 0.7$ $\rho = 0.26$.

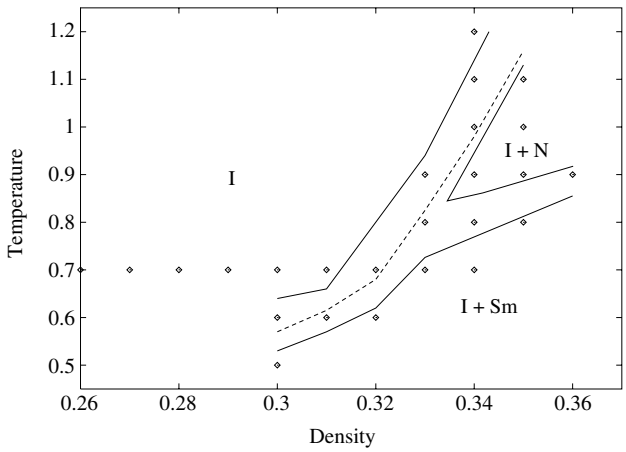

Figure 2. Partial phase diagram of the bulk 90/10 mixture. Diamonds indicate simulation points, full lines indicate approximate lines of phase stability and the broken line separates the homogeneous and phase-separated regions.

Table 1. Temperature dependence of the nematic order parameter, S, for the bulk 90/10 rod–sphere mixture at $\rho = 0.34$.

T	0.7	0.8	0.9	1.0	1.1
S	0.90 ± 0.01	0.65 ± 0.02	0.58 ± 0.02	0.41 ± 0.05	0.16 ± 0.03

On compression at this temperature, nematic order parameter and radial distribution function measurements indicated that the system remained well mixed and isotropic up to a density of about $\rho = 0.32$. At this point, phase separation was seen between sphere-rich isotropic and rod-rich smectic phases. A subsequent heating sequence, conducted at number density $\rho = 0.34$, gave the $S(T)$ behaviour shown in table 1. These data, supplemented by rod–rod pair correlation function measurements, indicate that as the temperature was increased the system underwent a smectic–nematic transition at $T \simeq 0.8$. On further heating, the nematic order parameter decreased further and, at $T \simeq 1.1$, dropped to values indicative of an isotropic phase. Based on these two simulation sequences and a number of additional runs (marked with diamonds) the partial phase diagram shown in figure 2 was constructed for this 90/10 mixture. While this contains all of the phases observed for the pure Gay–Berne fluid, it is noteworthy that, for the phase points investigated here, the onset of orientational ordering was always associated with phase separation. While this cooperative behaviour must break down at high temperatures, in order for the hard-particle limit to be regained, we shall see that the absence of a homogeneous nematic phase here for $T \leqslant 1.1$ provides an interesting comparison with the behaviour found when a colloidal particle is introduced.

We now consider the properties of this same 90/10 rod–sphere mixture (again, 2048 small particles in total) in the presence of a spherical colloid of radius $3\sigma_0$. For this, the interaction potentials introduced in section 2 require three energy parameters to be set: the strength and anisotropy of the colloid–rod interaction and the strength of the colloid–sphere interaction. Following the concept of the colloid being composed of smaller spheres, we have considered two cases of the colloid–rod interaction anisotropy: $\epsilon_E/\epsilon_S = 5.0$ and 0.2. These correspond, respectively, to radial and tangential anchoring. When these values were inserted into equation (9), $\epsilon_{CR}^{end}/\epsilon_{CR}^{side}$ was found to have a weak dependence on the colloid radius R. Thus,

Table 2. Simulation observables from the $T = 1.0$ compression sequence with the radially anchored colloid.

ρ	PE per particle	S
0.30	-2.756 ± 0.022	0.044 ± 0.014
0.31	-2.792 ± 0.024	0.058 ± 0.016
0.32	-2.845 ± 0.029	0.063 ± 0.018
0.33	-2.938 ± 0.029	0.183 ± 0.024
0.34	-3.037 ± 0.029	0.590 ± 0.022
0.35	-3.098 ± 0.031	0.688 ± 0.017

the values of $\epsilon_{\mathrm{CR}}^{\mathrm{end}}/\epsilon_{\mathrm{CR}}^{\mathrm{side}}$ for $R = 3\sigma_0$ were found to be 5.599 and 0.224 for $\epsilon_{\mathrm{E}}/\epsilon_{\mathrm{S}} = 5.0$ and 0.2, respectively.

In this model, the strength of, for example, the radial anchoring is largely determined by the well depth of the colloid–rod end interaction, $\epsilon_{\mathrm{CR}}^{\mathrm{end}}$. When this was made too deep (the case $\epsilon_{\mathrm{CR}}^{\mathrm{end}} = 5$ was tested), the rods simply formed a radially aligned shell around the colloid, effectively forming an enlarged colloid of diameter $12\sigma_0$. The absolute values of the colloid–rod interaction strengths were, therefore, scaled as follows. For the tangential anchoring case, ϵ_0^{CR} was adjusted to give $\epsilon_{\mathrm{CR}}^{\mathrm{side}} = 2.0\epsilon_0$ and $\epsilon_{\mathrm{CR}}^{\mathrm{end}} = 0.448\epsilon_0$. For the radial anchoring case, the scaling was set to provide $\epsilon_{\mathrm{CR}}^{\mathrm{side}} = 0.40\epsilon_0$ and $\epsilon_{\mathrm{CR}}^{\mathrm{end}} = 2.24\epsilon_0$. Note that, at $T \approx 1.0$, this gives colloid–rod interaction energies of the same order as $\frac{5}{2}T$, the average kinetic energy of a single rod. The strength of the colloid–sphere interaction parameter, ϵ_0^{CS}, was scaled in a similar way to provide an interaction well depth of ϵ_0 (compare to figure 1).

For the system with a radially anchored colloid, one compression sequence and one cooling sequence were performed. The initial configuration for this system was created from a bulk configuration of 2048 small particles by placing a colloidal particle of zero size in the simulation box and gradually expanding it up to $R = 3\sigma_0$. This system was then equilibrated for 7×10^6 time steps at $\rho = 0.30$ and $T = 1.0$, to give an isotropic and homogeneous configuration with little distortion at the colloid surface. This was compressed at $T = 1.0$ up to a number density of $\rho = 0.35$. The potential energy per particle and nematic order parameter values measured during this sequence are presented in table 2. These data indicate an isotropic–nematic transition at $\rho \approx 0.33$. Figure 3(a) shows the rod–rod and sphere–sphere radial distribution functions measured at $\rho = 0.35$ and $T = 1.0$. These indicate the homogeneity of this mixture, as do the corresponding configuration snapshot and director field map (figures 3(b) and (c)). To calculate the latter, the simulation box was divided into $30 \times 30 \times 30$ cells and the order parameter in each cell calculated as an average over 4×10^6 timesteps. Since, in the cases depicted here, the overall director was parallel to one of the simulation box sides, it was possible to simply slice the system through the centre of the colloid and calculate the order averaged over equivalent cells in the two central planes. Thus, the director field is displayed using ellipses whose orientations and eccentricities indicate the orientational order and whose greyscale colours indicate the local rod-number density.

While some disruption of the director field is apparent from figures 3(b) and (c), it did not prove possible to detect a stable defect structure in this system. This is presumably related to the relatively weak radial anchoring induced at the colloid surface. The most noteworthy aspect of this set of results is, therefore, its departure from the bulk phase behaviour of the 90/10 rod–sphere mixture: in the presence of the colloidal particle, the rod–sphere mixture has formed a homogeneous nematic phase, rather than phase separating. Since the colloid reduced the free volume available for the small particles (by occupying approximately 3.5% of the box), this mixture was expected to phase separate at $\rho = 0.34$. Instead, it remained

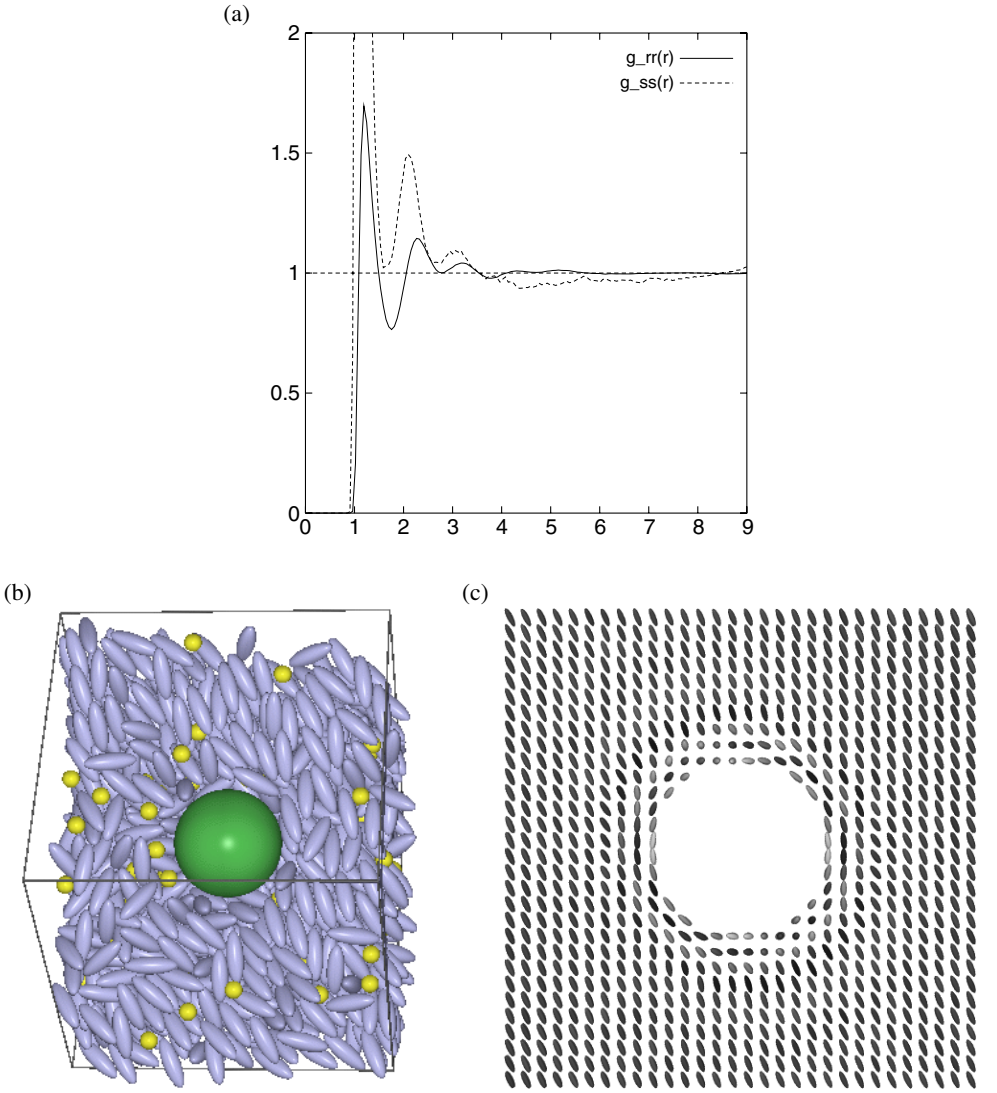

Figure 3. (a) Radial distribution functions $g_{rr}(r)$ and $g_{ss}(r)$ measured at $\rho = 0.35$ and $T = 1.0$ with the radially anchored colloid; (b) configurational snapshot and (c) director map obtained at this data point.

homogeneous even at $\rho = 0.35$. We infer from this that the elastic free energy gain obtained by the colloid-free 90/10 system when it phase-separated was restricted here by the director field distortions imposed by the colloid. This does not imply a change of phase behaviour due to the presence of a single colloidal particle, since the periodic boundary conditions used here imply a periodic array of such particles. Instead, it appears that the compositional homogeneity of this nematic phase followed from the inclusion of two types of spherical particles, with very different sizes, in the simulation. Taken in the context of recent experimental results [19, 20], this observation may help to explain why the transparent nematic phase reported by Yamamoto and Tanaka [21] has not been found in this newer work.

Table 3. Simulation observables from the $\rho = 0.34$ cooling sequence with the radially anchored colloid.

T	PE per particle	S
1.00	-3.037 ± 0.029	0.590 ± 0.021
0.95	-3.263 ± 0.028	0.626 ± 0.014
0.90	-3.582 ± 0.029	0.653 ± 0.002
0.85	-3.869 ± 0.033	0.692 ± 0.002

In order to induce a higher degree of radial alignment at the colloid surface, the system was subjected to a cooling sequence at $\rho = 0.34$. The results of previous studies [9, 10] indicate that, for this size of colloidal particle, increasing the anchoring strength should induce formation of a Saturn ring defect. While the potential energy and order parameter data from this cooling sequence (table 3) indicate reasonably steady changes, the corresponding radial distribution functions and configurational snapshots show phase separation for $T \leqslant 0.90$. Interestingly, the configurational snapshot and director map (figures 4(a) and (b)) show that, rather than nucleating into a Saturn ring structure (i.e. residing preferentially in the expected disordered region), the spheres clustered into a single, approximately spherical droplet. We ascribe the formation of this alternative droplet structure to the additional effect of the rod–sphere surface tension, which will have opposed any large-surface-area arrangement such as a ring of spheres. In general, we would expect the shape and dynamics of this droplet to vary with its size. For example, the effective attraction to equatorial regions might lead to a less spherical droplet were a larger number of small spheres included in the system.

To gain information on the behaviour of the droplet formed here, measurements were made of the probability distribution of small spheres resolved along the director. Here the number of spheres was calculated in slices perpendicular to the director and normalized by their volumes and the total number of spheres counted. Figure 4(c) shows the results for this distribution function averaged over 2×10^5 time steps at $T = 0.85$. It confirms that the spheres making up this droplet tended to reside in the equatorial plane of the colloidal particle. Distributions equivalent to that shown in figure 4(c) but averaged over shorter times were not symmetrical around zero (the equatorial plane), even though they resulted in a symmetrical distribution after averaging. This suggests that the droplet of spheres underwent marked oscillations away from its equilibrium position.

Due to the symmetry of the rod–sphere interaction (recall that the spheres favoured the sides of the rods) the droplet of spheres formed by this system was, effectively, a second colloid with tangential surface anchoring. Therefore, the snapshot figure 4(a) can be interpreted as a stable arrangement for two colloidal particles with different senses of surface anchoring. On closer examination of this snapshot and the corresponding director map, evidence of a Saturn ring defect can still be seen diametrically opposite the droplet of spheres. We speculate, therefore, that the arrangement depicted in figure 4(a) actually comprises a radially anchored colloid with a Saturn ring defect which penetrates (and passes through the centre of) a coupled but distorted tangentially anchored colloid. Had two rigid colloids with opposing (i.e. normal and tangential) anchoring conditions achieved twinning in this way, in so doing they would have had to overcome a mutual repulsion due to the (elastically expensive) hybridly anchored region that would have developed between them. We suggest, therefore, that the sequence of events that lead to the formation of the twinned structure may here have involved an initial nucleation of the small spheres at (and promoted by) the ring defect. In this scenario, the preferred anchoring of the tangential colloidal will not have played a role until the droplet location was reasonably well established. The boojum defects associated with the tangential

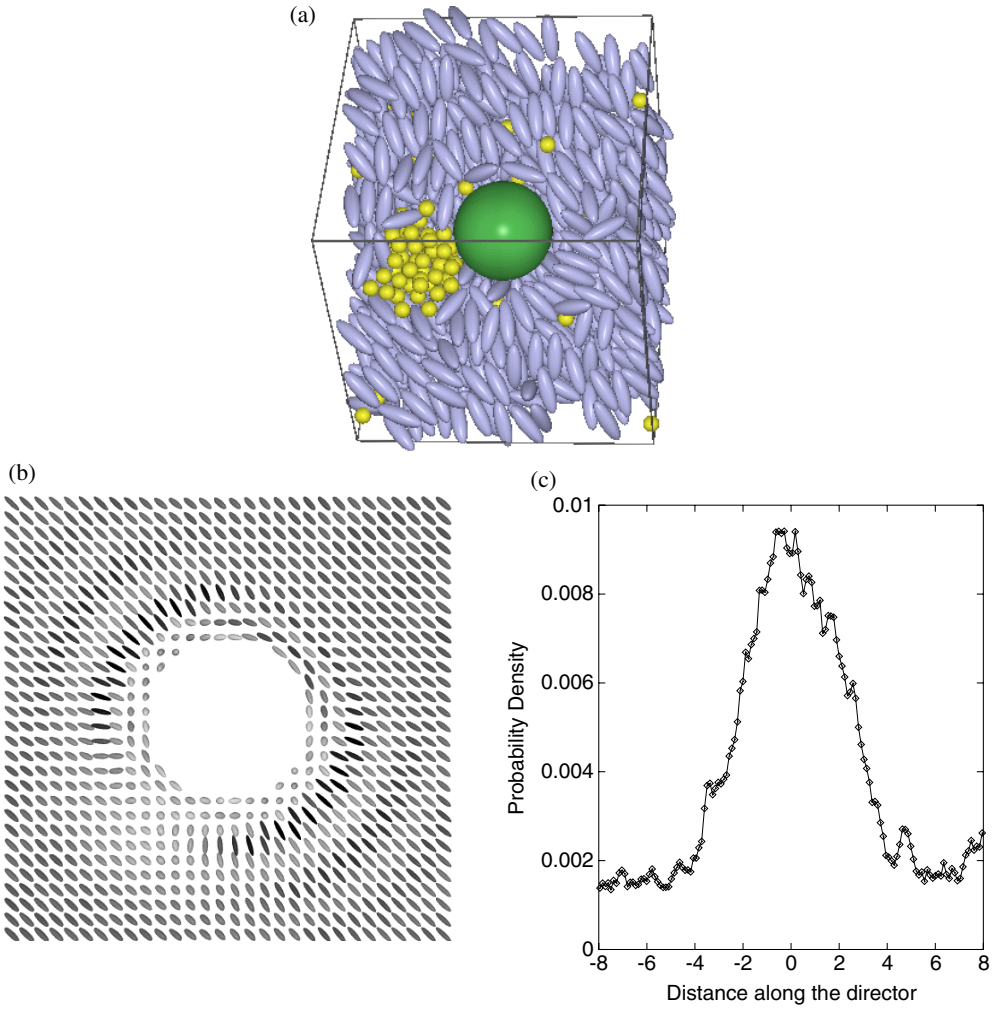

Figure 4. (a) Configurational snapshot and (b) director map obtained at $\rho = 0.34$ and $T = 0.85$; (c) probability distribution of small spheres along the director at this state point (centred on the colloid equatorial plane).

colloid [22] can also be seen in figure 4(a) on the bisector of the two colloid centres. On the basis of these observations, we have constructed the schematic diagram of a possible director field for this arrangement given in figure 5.

Finally, the same 90/10 rod–sphere mixture was simulated with a colloidal particle parametrized to favour tangential anchoring. Analogous to the simulations discussed above, this system was first compressed at $T = 1.0$ through the density range $0.30 \leqslant \rho \leqslant 0.35$. The potential energy per particle and nematic order parameter values measured during this sequence are shown in table 4. These indicate an isotropic–nematic transition, the presence of the colloid again inhibiting the tendency of the small spheres to phase separate. Subsequently, the final configuration obtained at $\rho = 0.35$ was cooled to $T = 0.85$ with a decrement of $\Delta T = 0.05$. According to the sphere–sphere radial distribution function data, this system underwent phase separation at $T = 0.90$. Here, the probability distribution of small spheres along the director

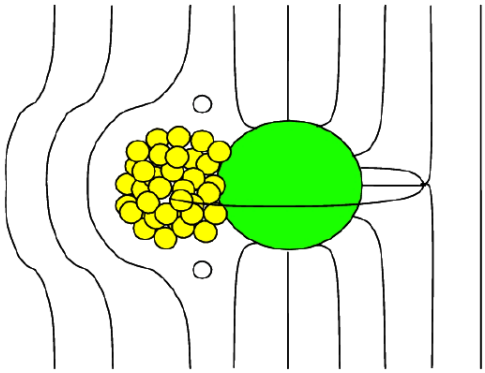

Figure 5. Schematic diagram of the director field corresponding to the configuration snapshot shown in figure 4(a).

Table 4. Simulation observables from the $T = 1.0$ compression sequence with the tangentially anchored colloid.

ρ	PE per particle	S
0.30	-2.761 ± 0.024	0.044 ± 0.016
0.31	-2.834 ± 0.026	0.068 ± 0.018
0.32	-2.901 ± 0.027	0.125 ± 0.031
0.33	-2.982 ± 0.029	0.455 ± 0.017
0.34	-3.061 ± 0.029	0.581 ± 0.018
0.35	-3.129 ± 0.034	0.678 ± 0.019

(figure 6(a)) indicated clustering of spheres near to the poles of the colloid. The configuration snapshot and director map obtained at $\rho = 0.35$ and $T = 0.9$ (figures 6(b) and (c)) illustrate the resulting structure for this case, a droplet of spheres being located adjacent to each of the colloid's poles.

Here, therefore, the simulation results gave an outcome consistent with expectations: the spheres aggregated preferentially in the orientational defect regions. The reason for the clustering of the spheres at the boojums is simply that such an arrangement expels LC particles from a region in which there would otherwise have been a high elastic free energy density. The 'melting' of these defect regions by isotropic particles also has implications for the director-field-mediated colloid–colloid interactions present in a more general multi-colloid setup since, for example, the long-ranged form and dynamic response of a melted defect will presumably differ from those of a true LC defect. As yet, we are not aware of any published work on experimental investigations of such effects.

4. Conclusions

In this paper, we have extended our previous work on mixtures of small spheres and rods by incorporating an additional large spherical particle. This has been achieved through the development of an efficient potential for the interaction between small particles and a large spherical particle. This potential also provides an intuitive link between model parameters and the sense and strength of the surface anchoring.

Here, exploratory simulations have shown that the incorporation of a spherical colloidal particle (and its periodic images) can change the bulk phase behaviour of the surrounding rod–

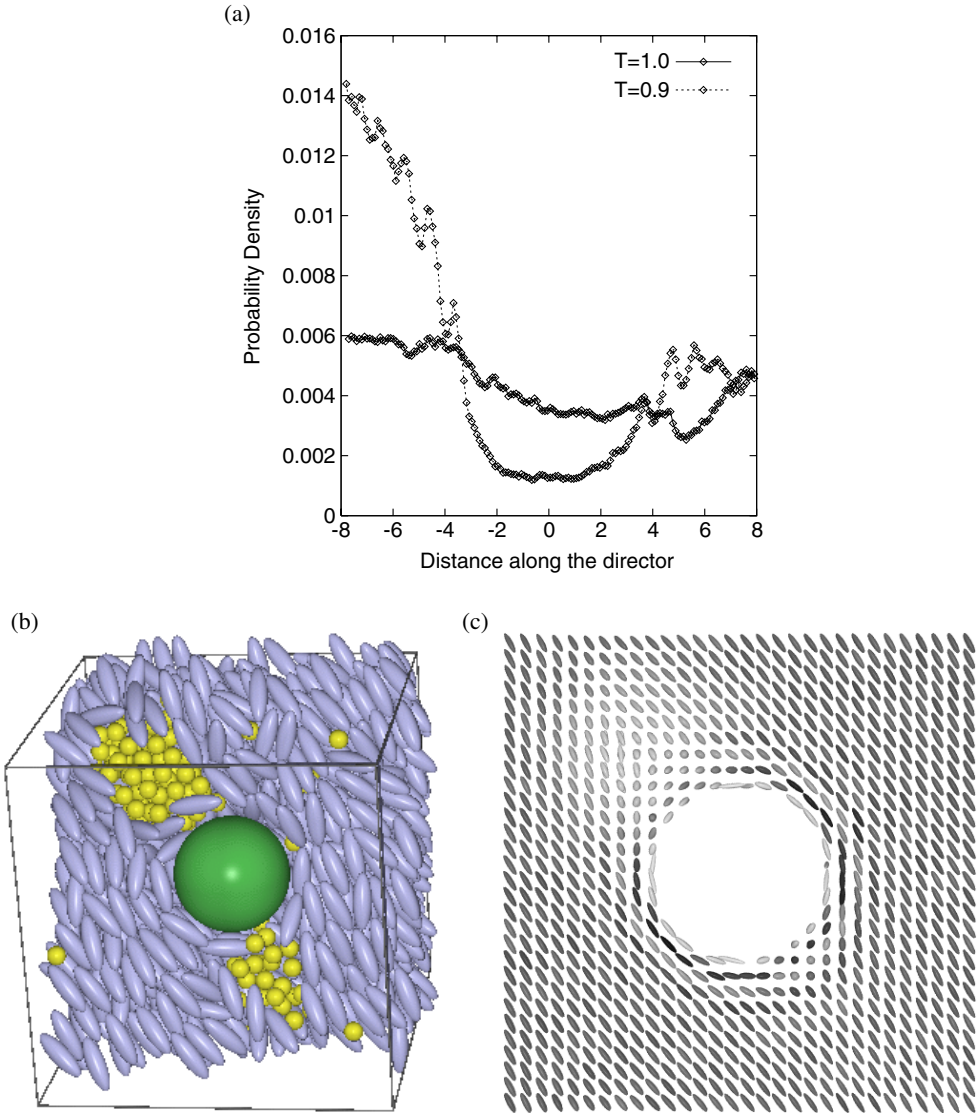

Figure 6. (a) Sphere probability distribution along the director at $\rho = 0.35$ and $T = 1.0$ and 0.9; (b) configurational snapshot and (c) director map obtained at the lower temperature.

sphere solvent. Additionally, the presence of the small spheres in the solvent has been shown to modify the defect structures formed by both radially and tangentially anchoring colloids. In the latter case, the effect was relatively minor, in that the spheres simply clustered at the defects, but in the former situation, the structure and symmetry of the director field around the colloid were both changed.

The range of changes observed here, in a relatively cursory survey of this class of system, suggests a rich phenomenology which is ripe for further exploration by both experiment and molecular simulation. Particularly fruitful areas for such studies include the use of small particulates for the control of LC-mediated colloid–colloid interactions (and thus the structures

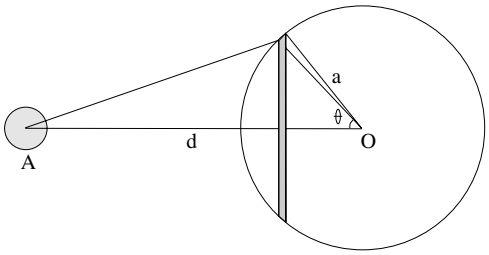

Figure 7. Schematic diagram of a spherical particle near a colloid.

adopted by LC colloids) and the possible range of structures formed when mixtures of colloids with different anchoring strengths and symmetries are incorporated into a LC solvent. The latter situation could also be generalized to the behaviour of surface-patterned LC colloids.

Acknowledgments

We thank Chris Care for useful discussions throughout this work. We gratefully acknowledge the financial support of the MRI in providing a studentship for DA, and EPSRC for providing computational hardware under grant GR/L86135.

Appendix

The colloid–sphere potential is defined as being the Lennard-Jones potential integrated over the colloid volume. To determine this, we first evaluate the interaction between a spherical shell of radius a and a Lennard-Jones sphere a distance r from the centre of the shell. To simplify the algebra, the interaction is initially considered here to be proportional to $\epsilon_0(\frac{\sigma_0}{r})^n$. The points located on a ring on the sphere given by constant θ and $0 \leqslant \phi < 2\pi$ are equidistant from point A, the location of the Lennard-Jones sphere (figure 7). If da is the thickness of the spherical shell and $a\,\mathrm{d}\theta$ is the width of the ring, the potential created by this ring at the point A is:

$$\mathrm{d}U\,(r,a,\theta) = \int_0^{2\pi} \frac{\epsilon_0{\sigma_0}^n a\,\mathrm{d}\theta\,\mathrm{d}a\,\rho a\sin\theta\,\mathrm{d}\phi}{(r^2+a^2-2ar\cos\theta)^{n/2}} \tag{13}$$

where the constant $\rho = \frac{N_{\mathrm{total}}}{4\pi a^2\,\mathrm{d}a}$ is the number density of the microscopic particles assumed to make up the colloid. Integrating dU over angular variables (i.e. the whole spherical surface) gives

$$U(r,a) = \frac{N_{\mathrm{total}}\epsilon_0{\sigma_0}^n}{2ar(n-2)}\left[\frac{1}{(r-a)^{n-2}} - \frac{1}{(r+a)^{n-2}}\right], \qquad n \neq 2. \tag{14}$$

The potential created at A by the full colloid is then given by the sum of the contributions from a set of concentric spherical shells. In order to calculate this, we integrate $U(r,a)$ over radii in the range $0 \leqslant a \leqslant R$ to obtain

$$U(r) = \frac{2\pi\rho\epsilon_0{\sigma_0}^n}{r(n-2)}\left[\frac{r}{n-3}\left(\frac{1}{(r-R)^{n-3}} - \frac{1}{(r+R)^{n-3}}\right) - \frac{1}{n-4}\left(\frac{1}{(r-R)^{n-4}} - \frac{1}{(r+R)^{n-4}}\right)\right].$$

In the vicinity of the colloid's surface, $(r - R) \ll (r + R)$ and terms containing $(r + R)$ in their denominator can be neglected for sufficiently large n. For exponents $n = 6$ and 12, this approximation is reasonable and the resultant expression for the colloid–sphere potential is

$$U^{\mathrm{CS}}(r) = \epsilon_{\mathrm{CS}} \left[\frac{1}{45} \left(\frac{\sigma_0}{r - R} \right)^9 - \frac{1}{6} \left(\frac{\sigma_0}{r - R} \right)^3 - \frac{\sigma_0}{40r} \left(\frac{\sigma_0}{r - R} \right)^8 + \frac{\sigma_0}{4r} \left(\frac{\sigma_0}{r - R} \right)^2 \right], \quad (15)$$

where ϵ_{CS} is now taken to be an adjustable parameter which depends on the packing of particles forming the colloid and the strengths of their interactions with an external particle.

References

[1] Asakura S and Oosawa F 1958 *J. Polym. Sci.* **33** 183
[2] Vliegenthart G A, van Blaaderen A and Lekkerkerker H N W 1999 *Faraday Discuss.* **112** 173
[3] Mao Y, Cates M E and Lekkerkerker H N W 1997 *J. Chem. Phys.* **106** 3721
[4] Kuksenok O V, Ruhwandl S V and Terentjev E M 1996 *Phys. Rev.* E **54** 5198
[5] Stark H 1999 *Eur. Phys. J.* B **10** 311
[6] Ruhwandl R W and Terentjev E M 1997 *Phys. Rev.* E **56** 5561
[7] Yamamoto R 2001 *Phys. Rev. Lett.* **87** 075502
[8] Good K 2001 *PhD Thesis* Sheffield Hallam University
[9] Billeter J L and Pelcovits R A 2000 *Phys. Rev.* E **62** 711
[10] Andrienko D, Germano G and Allen M P 2001 *Phys. Rev.* E **63** 041701
[11] Pikin S A and Terentjev E M 1988 *Crystallography* **33** 1084
[12] Voloschenko D, Pishnyak O P, Shiyanovskii S V and Lavrentovich O D 2002 *Phys. Rev.* E **65** 060701(R)
[13] Gay J G and Berne B J 1981 *J. Chem. Phys.* **64** 3316
[14] De Miguel E, Rull L F, Chalam M K and Gubbins K E 1991 *Mol. Phys.* **74** 405
[15] Berne B J and Pechukas P 1972 *J. Chem. Phys.* **56** 4213
[16] Barmes F, Webster R E and Cleaver D J 2004 in preparation
[17] Allen M P and Tildesley D J 1986 *Computer Simulation of Liquids* (Oxford: Oxford University Press)
[18] Antypov D and Cleaver D J 2003 *Chem. Phys. Lett.* **377** 311
[19] Zalar B, Lalar S and Žumer S 2003 *ESF Exploratory Workshop on Liquid Crystal Colloid Dispersions (Bled, 2003)*
[20] Bellini T, Caggioni M, Clark N A, Mantegazza F and Maritan A 2003 *ESF Exploratory Workshop on Liquid Crystal Colloid Dispersions (Bled, 2003)*
[21] Yamamoto J and Tanaka H 2001 *Nature* **409** 321
[22] Loudet J, Barois P and Poulin P 2000 *Nature* **407** 611